







# Retinal neurovascular coupling evaluation with circular-scan OCTA

NAIXING HUANG,<sup>1,2</sup>  TRISTAN T. HORMEL,<sup>1</sup> SIYU CHEN,<sup>1,2</sup>   
DAVID HUANG,<sup>1,2</sup>  THOMAS S. HWANG,<sup>1</sup> STEVEN T. BAILEY,<sup>1</sup> AND  
YALI JIA<sup>1,2,\*</sup> 

<sup>1</sup>Casey Eye Institute, Oregon Health & Science University, Portland, Oregon, USA

<sup>2</sup>Department of Biomedical Engineering, Oregon Health & Science University, Portland, Oregon, USA

\*jiaya@ohsu.edu

**Abstract:** Neurovascular coupling (NVC) is the mechanism by which neuronal activity regulates blood flow. Detection of abnormalities in NVC may be clinically useful as they could signal early retinal dysfunction before structural damage becomes apparent. While optical coherence tomography angiography (OCTA) enables high-contrast, non-invasive functional imaging of the retina, its conventional form cannot detect light-evoked hemodynamic responses, which are the key indicators of NVC. Visualizing and quantifying NVC-driven hemodynamics in the human retina remains challenging due to motion artifacts and insufficient temporal resolution. To overcome these limitations, we developed a functional OCTA prototype integrated with a green light stimulus that reliably triggered NVC. The OCTA prototype was built with off-the-shelf optics and a 200-kHz A-line rate laser to assess NVC *in vivo* with a circular-scan pattern to improve the temporal resolution and reduce motion artifacts. We present NVC response curves and statistical analyses across multiple vascular plexuses in healthy eyes, demonstrating the system's potential for both clinical translation and advancing early diagnosis of retinal diseases.

© 2025 Optica Publishing Group under the terms of the [Optica Open Access Publishing Agreement](#)

## 1. Introduction

Blood flow autoregulation is linked to neuronal activity, ensuring metabolic demand is met. This process is conceptualized as neurovascular coupling (NVC) [1]. Recently, studies have proposed several biochemical cascades underlying NVC [2], further elucidating the role of blood flow changes in both normal and impaired NVC. The retina has observable vasculature *in vivo* with neural cells that can be activated using light stimulus, which makes it an ideal candidate for NVC evaluation. Furthermore, common eye diseases such as diabetic retinopathy and age-related macular degeneration have known interactions between the vessels and the neural tissue. The loss of photoreceptors in age-related macular degeneration, for example, is associated with the loss of choriocapillaris and a decrease in deep capillary plexus [3]. In diabetic retinopathy, loss of pericytes and endothelial cells are associated disorganization of the neuronal cell layers and loss vision [4]. In these conditions, NVC impairment could precede observable anatomic changes in neuronal tissue or the vasculature. Therefore, NVC evaluation could elucidate the pathophysiology in the early stages of disease, allow earlier detection of disease as well as potential therapeutics that target the early stage before permanent anatomic changes occur.

NVC evaluation in the retina requires a light stimulus to elicit neuronal activity and the ability to detect changes in hemodynamic processes such as vasodilation or a change in flow velocity [1]. Polak et al. described a retinal vessel analyzer to evaluate NVC by measuring vessel diameter in response to light flicker, but its sensitivity was limited to larger vessels [5]. Srien et al. built an experimental system with confocal microscopy and laser speckle flowmetry imaging smaller vessels (Fig. 1(B), (D)) [6]. Although the vasodilation and velocity increase (Fig. 1(C), (E)) were successfully visualized and quantified, it has not been applied to human eye imaging due to its complexity of ocular alignment. Adaptive optics scanning laser ophthalmoscopy enables

*in vivo* imaging with high spatiotemporal resolution, which has provided valuable insights into capillary-level NVC [7], but it is time-consuming and impractical for clinical use.

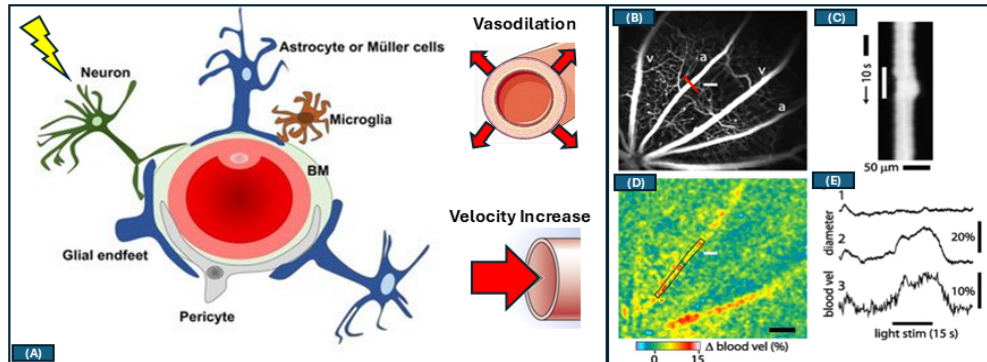


**Fig. 1. Neurovascular coupling (NVC) in response to light stimulus.** (A) Schematic. The light stimulus activates retinal neurons and other cells, increasing metabolic demand. In response, blood flow autoregulation enhances the blood supply through vasodilation and velocity increase. BM: Basement membrane. (B)-(E) NVC-driven hemodynamics measurement with confocal microscopy and laser speckle flowmetry on rat retina. (B) Confocal image of retinal vessels, with arteriole diameter measured along the red line. The white bar marks the flickering light stimulus location (also in (D)). (C) Line scan image of the arteriole in (B), showing vessel dilation in response to flickering light (white bar). (D) Blood velocity ratio image showing increased velocity in arterioles and smaller changes after stimulus. (E) NVC response curves visualizing the vessel diameter and velocity change. (A) was reproduced from Fragiotta et al. [8] and (B)-(E) were reproduced from Srienc et al. [6] with permission.

Optical coherence tomography (OCT) angiography (OCTA), built on the OCT platform, can cross-sectionally and volumetrically visualize vasculature down to capillary scale with high repeatability [9]. Based on that advance, NVC evaluation with OCTA can potentially resolve these unmet imaging needs within clinical practice. The first NVC evaluation study using OCTA in the human eye was reported by Wei et al., who visualized NVC-driven hemodynamics from continually acquired OCTA volumes [10]. However, at ophthalmic OCTA speed, volumetric scan patterns are highly susceptible to motion artifacts from microsaccades and blinks in prolonged imaging, posing challenges for spatiotemporal analysis of NVC-driven hemodynamics. Even with 3D strip-based registration, significant eye movements between volumes can lead to irrecoverable regions [11,12]. Other clinically translatable studies mitigate this issue by reducing the number of OCTA volumes captured during prolonged imaging [13]. While these approaches simplify the imaging procedure, they limit detailed observation of temporal dynamics, differentiating individuals, and repeatability validation. Therefore, an alternative method for NVC evaluation is needed.

Parafoveal vasculature is critical for central vision, high acuity, and color perception [14]. Given the circular symmetry of parafoveal vessel geometry, we propose that a circular-scan pattern would solve unmet temporal resolution challenges for NVC evaluation by simultaneously acquiring the hemodynamics from all small vessels in the parafovea. In this study, we developed a clinically translatable OCTA system with a circular scanning pattern and introduced a data post-processing method to remove artifacts during prolonged imaging, thus enhancing the sensitivity of NVC evaluation. We demonstrated NVC response curves in healthy eyes and performed visualization and quantification across different vascular plexuses, offering new insights into retinal NVC.

## 2. Methods

### 2.1. Study population and inclusion criteria

This pilot, observational study recruited and imaged adult participants without a known history of retinal disease at the Casey Eye Institute. The research protocol was approved by the OHSU institutional review board (Approval number: IRB 00008456) and carried out in accordance with the Declaration of Helsinki. Written informed consent was obtained from each participant before the start.

### 2.2. Functional OCTA system specifications

A previously developed 1060-nm 200-kHz swept-source OCT prototype [15] was integrated with a Pico projector (Ultra Mini, KODAK) for NVC evaluation (Fig. 1(A)). The optical system included objective and ocular lenses, designed as two achromatic doublet pairs to minimize spherical aberrations. OCT delivered a 2.2 mm ( $1/e^2$ ) diameter OCT beam on the cornea, resulting in a 10  $\mu$ m lateral resolution on the retina. The laser power at the cornea was measured at 1.8 mW, complying with ANSI Z136.1-2014 standards for 1060-nm light. A numerical  $k$ -sampling method was implemented for OCT signal processing to replace the unstable  $k$ -clock [16]. Additionally, a sweep trigger signal was used to drive the galvo scanner to perform a circular-scan pattern for improved NVC evaluation [17]. A green light was co-aligned with the OCT beam and projected onto the retina with a 10-Hz frequency and 80% duty cycle, triggering the NVC function. The green light beam diameter on the retina was experimentally determined as 6 mm (86% of the aperture) using an eye calibrator positioned at the pivot point of the OCT scan. The calibrator consisted of a 19-mm focal length lens and a beam profiler (Beam Profiler 4 M, Edmund Optics). The stimulus beam square is sufficient to fully stimulate the parafoveal region. Green light power was measured to be 7.32  $\mu$ W/cm<sup>2</sup> on the cornea. Wavelengths range from 515 to 530 nm. The software modulating the duration and frequency of stimulation was programmed with the HDMI library in C++. A red dot was displayed at the stimulus center to act as a fixation target. The maximum sensitivity was measured to be 102.2 dB, with 2.3-dB roll-off measured at 4 mm from the zero-delay. 20 mrad of phase variation at 1.1 mm from the zero-delay was estimated. The axial point spread function of our system, as measured in the dB scale at 1.1 mm from the zero-path delay, yielded a maximum axial resolution of 4.9  $\mu$ m in air. *En face* OCTA images of superficial vascular complex and choriocapillaris demonstrated capillary-level resolution, confirming the system was well-calibrated (Fig. 2(B), (C)).

### 2.3. Imaging protocol and data acquisition

Enrolled subjects were dark-adapted for 5 minutes, followed by 36-second imaging, then followed by a 10-minute break. The 36 seconds for imaging/NVC evaluation included three sequential sessions: 8-second baseline, 15-second stimulation, and 13-second post-stimulation. Participants were instructed to blink freely but to limit blinking to every 3–4 seconds and refocus on the fixation target after movement. Each participant underwent three repeated evaluations for each eye as one trial. Pupil dilation was not required.

A circular-scan pattern with a 1.5 mm diameter was applied to enable simultaneous scanning across all small vessels in the parafovea and avoiding the foveal avascular zone (Fig. 3(A)). The circumference of each circular B-scan is 4.71 mm. Circular B-scans were sampled at a density of 800 A-lines per OCT B-scan and 10080 OCT B-scans per NVC evaluation, approximate to a Nyquist-sampling transverse pixel size of 5.8  $\mu$ m (Fig. 3(B)). The NVC evaluation commenced once optimized focusing and retinal positioning were confirmed in the real-time OCT software display. Circular OCT B-scans were continually acquired at a frame rate of 250-Hz and converted into an OCTA time course in data post-processing.

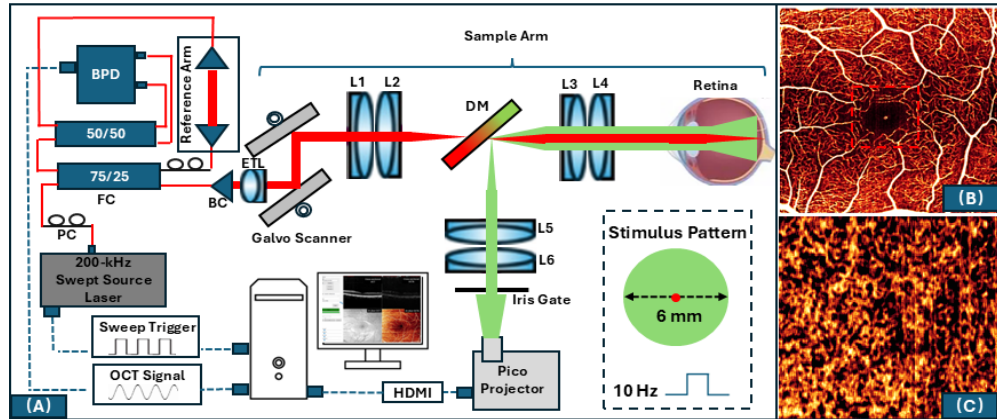


**Fig. 2. System design and performance.** (A) Functional OCTA system schematic. Light from a 200-kHz swept-source laser is split by a 75/25 fiber coupler (FC), with 25% directed toward the retina (red light trace). Lenses L1-L2 and L3-L4 are both achromatic doublet pairs with effective focal lengths of 37.5 mm and 50 mm, ensuring high optical resolution. In the sample arm, electrically tunable lenses (ETL), placed after the beam collimator (BC), dynamically adjust the OCT beam focus on the retina. The reference arm incorporates a delay line to match the optical path length in the sample arm. The OCT signal is converted to an electronic signal by a balanced photodetector (BPD) and digitized for real-time processing on a personal computer. The green light travels through the iris gate, dichroic mirror (DM), and lenses L5-L6 and L3-L4 to the retina (black dashed box). (B)-(C) Imaging performance. *En face* OCTA of the superficial vascular complex (B) and choriocapillaris (C) in the zoom-in region (red dashed box) demonstrate high-resolution imaging enabled by the system.

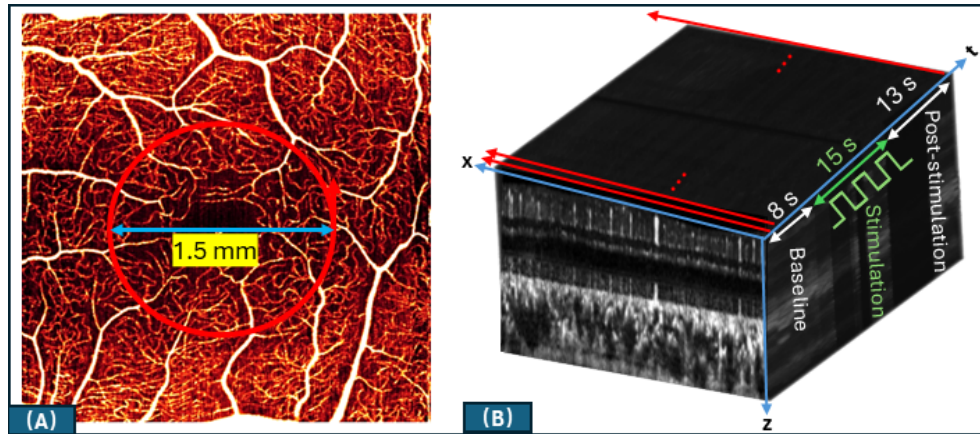


**Fig. 3. Circular-scan pattern and data acquisition.** (A) The circular scanning trajectory (red circle) with a 1.5 mm diameter (blue double arrow) is overlaid on an *en face* superficial vascular complex angiogram for illustration. (B) Sequential OCTA over entire time course. The circular OCTA B-scan shows lateral (x), depth (z), and temporal (t) coordinates. The OCTA stack consists of a group of circular OCTA B-scans, continuously recording the hemodynamics of all parafoveal vessels over the baseline, stimulation, and post-stimulation.

#### 2.4. Data post-processing

Our data post-processing involved three major steps: OCT-OCTA time course generation, artifact removal, and NVC amplitude calculation (Fig. 4). The OCT-OCTA time course generation



outputs temporally ordered and registered OCT and OCTA B-scans. The OCTA time course refinement utilizes the histogram of the OCT and OCTA time course to remove the B-scans with large motion and vignetting artifacts. Additionally, OCTA projection artifacts are removed for accurate measurement. After refinement, NVC amplitude calculation averages the artifact-free OCTA time course into an NVC response curve as a single evaluation. We describe each of these steps in detail below.

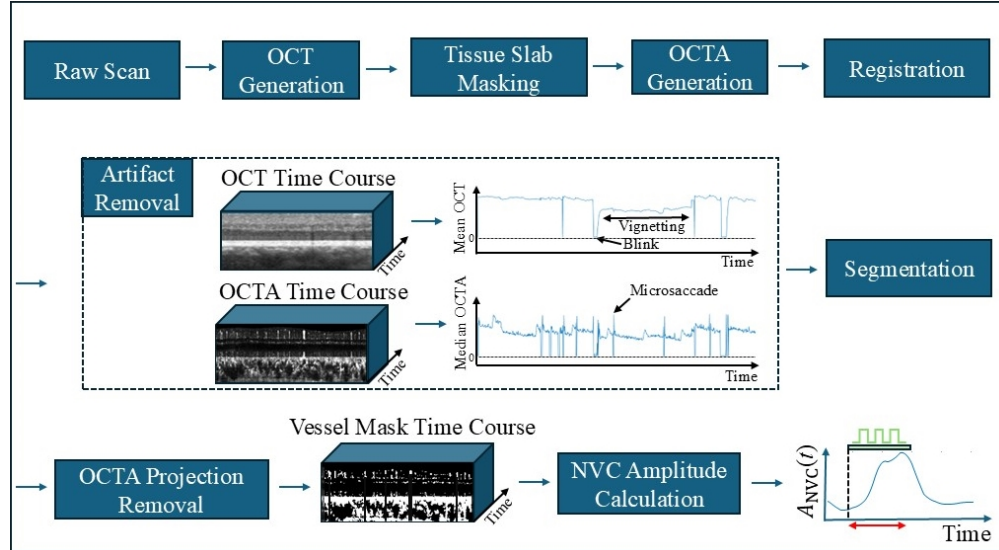


**Fig. 4. Data post-processing for NVC evaluation.** Post-processing begins with OCT and OCTA generation. OCT and OCTA B-scans were axially and laterally aligned using a 2D cross-correlation algorithm and flattened during registration. Artifact removal follows, identifying blinks, vignetting, and microsaccades using a  $[\text{mean}] \pm [\text{standard deviation}]$  threshold. After segmentation, OCTA projection artifacts are corrected with slab subtraction. Finally, the NVC response curve is obtained by applying NVC amplitude calculation to the refined OCTA time course, showing NVC amplitude and time-to-peak (red double arrow).

The first step, OCT-OCTA time course capture, begins with OCT generation, previously described in our earlier work [10]. Tissue slab masking removes background noise in OCT and OCTA time courses with a fixed threshold defined by the mean background amplitude. The second step is OCTA generation, where OCTA B-scans are obtained through 3 repeat scans at the same location. In particular, the phase-stabilized complex decorrelation algorithm is applied to improve the dynamic range, thus reducing the potential OCTA signal saturation for accurate hemodynamic measurements [18]. Raw OCTA B-scans are then procured into a time course using a consecutive processing window over time. A 2D normalized cross-correlation algorithm is applied to axially align all OCT and OCTA B-scans to the first reference B-scan and laterally align each B-scan to the preceding scan. To simplify OCTA plexus segmentation, OCT and OCTA B-scans are flattened by aligning each A-line with the first A-line, ensuring that the retinal pigment epithelium layer remains at a consistent depth across the B-scan [11]. Artifacts in the time courses will be removed in subsequent steps.

Next, we refine the OCT and OCTA time courses. Several artifacts in the time courses can be estimated using a regression-based algorithm [19]. For example, microsaccades can be identified by the dramatically increased median decorrelation value in an OCTA B-scan. In contrast, blink is estimated as an abnormally decreased mean intensity in an OCT B-scan as no OCT signal is detected. In addition to eye motion, the pupillary light reflex resulted in detrimental vignetting

[20], manifesting as a shadow-like attenuation on the OCT B-scan. Temporal curves of mean OCT intensity and median OCTA signal were generated separately. Thresholds based on the mean  $\pm$  standard deviation (SD) of each curve were applied to identify and discard B-scans affected by artifacts. The superficial vascular complex (SVC), intermediate capillary plexus (ICP), and deep capillary plexus (DCP) are segmented according to previously established definitions [21]. Slab subtraction was applied to remove projection artifacts on cross-sectional OCTA of the ICP and DCP [22]. The resulting artifact-free OCTA time course is then used for NVC amplitude calculation.

The last step is the NVC amplitude calculation. Vessel density (VD) was proposed as a blood flow quantification metric calculated with OCTA decorrelation value [10]. In this study VD is calculated based on OCTA B-scan instead of *en face* OCTA. To generate vessel masks for suppressing decorrelation noise from avascular tissue, a threshold is defined as the mean OCTA decorrelation value of the baseline plus two times its SD. Vessel mask is then calculated as

$$V(x, z, t) = \begin{cases} 1, & D(x, z, t) \geq \mu_{D(B)} + 2\sigma_{D(B)} \\ 0, & D(x, z, t) < \mu_{D(B)} + 2\sigma_{D(B)} \end{cases} \quad (1)$$

where  $V(x, z, t)$  is the vessel mask for each OCTA B-scan with the lateral  $x$ , depth  $z$ , and temporal  $t$  coordinates,  $D(x, z, t)$  is the OCTA decorrelation value.  $\mu_{D(B)}$  and  $\sigma_{D(B)}$  are the mean and SD of all decorrelation values of OCTA time course at the baseline. By summing the masked OCTA decorrelation value from all coordinates at the selected slab, VD is then obtained as

$$VD(t) = \frac{\sum_{x=1}^X \sum_{z=1}^Z V(x, z, t)}{XZ} \quad (2)$$

where  $VD(t)$  is the VD at the certain time point,  $X$  represents the B-scan length, while  $Z$  denotes the depth. Following the obtained VD, NVC amplitude is then acquired as the VD change by comparing it to its baseline average.

$$A_{NVC}(t) = \frac{VD(t) - \mu_{VD(B)}}{\mu_{VD(B)}} \times 100\% \quad (3)$$

where  $A_{NVC}(t)$  (%) is the NVC response curve reflecting the amplitude of NVC-driven hemodynamics,  $\mu_{VD(B)}$  is the mean value of VD during baseline. A 2.4-second averaging window and a Hampel filter (MATLAB) with a 3-neighbors measurement window are applied to smooth the residual spikes in the curve. Linear interpolation is used to fill empty data points in the curve caused by artifact scans. Curves with over 30% artifact scans were excluded from repeated evaluations, ensuring data quality. The repeated curves are then averaged for each eye. Time-to-peak (second) is then measured as the time from the start of stimulation to the point of maximum amplitude.

To test the robustness of the proposed circular-scan pattern in NVC evaluation, we modified a line-scan pattern by using a 1.2 mm line over the parafoveal region. A comparison between circular-scan and line-scan patterns was made, focusing on VD change at baseline. Line-scan B-scans were sampled at a Nyquist limit density of 240 A-lines per OCT B-scan and 7467 OCT B-scans, with OCTA B-scans acquired by processing 6 repeats using the same OCTA generation method as described in 2.4. The SD of NVC amplitude (%) in the baseline period was used to characterize the noise, reflecting the artifact signal caused by eye movements. The mean value and variation of noise were calculated from the noise data of all individuals.

### 3. Results

#### 3.1. Noise level is lower in circular B-scans

The study enrolled 9 healthy subjects (17 eyes), with an average age of  $33.4 \pm 4.0$  years (5 males, 4 females). We collected 51 imaging sets with the circular-scan pattern and 49 with the line-scan pattern. The artifact distribution map indicated that NVC response curves with over 30% artifact could be identified and discarded with the proposed artifact removal step (Fig. 5(A)). The result (Fig. 5(B)) showed that the artifacts portion in two scan patterns are similar ( $17.99\% \pm 13.61\%$ , circular-scan pattern;  $20.96\% \pm 12.47\%$ , line-scan pattern). After the artifact removal step, 29 curves were left in the circular-scan pattern, and 29 curves remained in the line-scan pattern. However, noise was reduced by around 14% with the circular-scan pattern ( $8.17\% \pm 6.82\%$ ) compared line-scan pattern ( $22.33\% \pm 20.01\%$ ), (Fig. 5(B)). The results suggest that the circular-scan pattern, by avoiding locational change such as scanning over the foveal avascular zone (Fig. 5(C)), is more robust than the line-scan. Preliminary results from the artifact removal step and scan pattern comparison can collectively validate the efficacy of circular-scan OCTA for NVC evaluation.

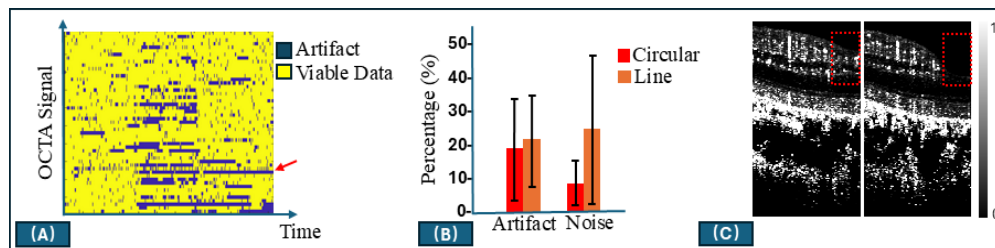


**Fig. 5. Artifacts in two different scan patterns.** (A) Artifact distribution map (circular-scan data) visualizing the artifacts over time, highlighting one with over 30% artifact (red arrow). (B) Bar plots depicting the comparison between circular-scan and line-scan patterns, indicating the noise in NVC evaluation is reduced with circular-scan pattern. (C) Line-scan OCTA examples without (left) and with (right) scanning over the foveal avascular zone, explaining locational change causes flow signal loss (red dashed box), resulting in noise.

#### 3.2. Visualization of NVC-driven hemodynamics

Individual differences were visually apparent in the NVC response curves (Fig. 6(A), (B)). One eye was excluded due to no usable curves after artifact removal. Among the 16 evaluated eyes, 11 exhibited peak NVC amplitude during stimulation, while 3 showed it during post-stimulation. The remaining 2 eyes didn't exhibit a significant increase in NVC amplitude. By averaging individual curves, a group evaluation was conducted to generate the NVC pattern (Fig. 6(C)). Representative OCTA B-scans provided cross-sectional perfusion changes across different NVC evaluation sessions, further validating the trend observed in the NVC pattern (Fig. 6(D1)–(D3)).

#### 3.3. Plexus-specific NVC amplitude

Adjusting the targeted slab in data post-processing enables the measurement of NVC amplitudes across different vascular plexuses. Averaged NVC patterns of the SVC, ICP, and DCP were obtained and visualized using color-coded plots (Fig. 7). Among these plexuses, the DCP exhibited the highest NVC amplitude in stimulation, followed by the ICP with an intermediate amplitude, while the SVC showed the lowest. The pronounced response in the DCP may be attributed to its proximity to the photoreceptor layer. Despite differences in amplitude, the temporal dynamics were largely synchronized: NVC amplitude of each plexus simultaneously

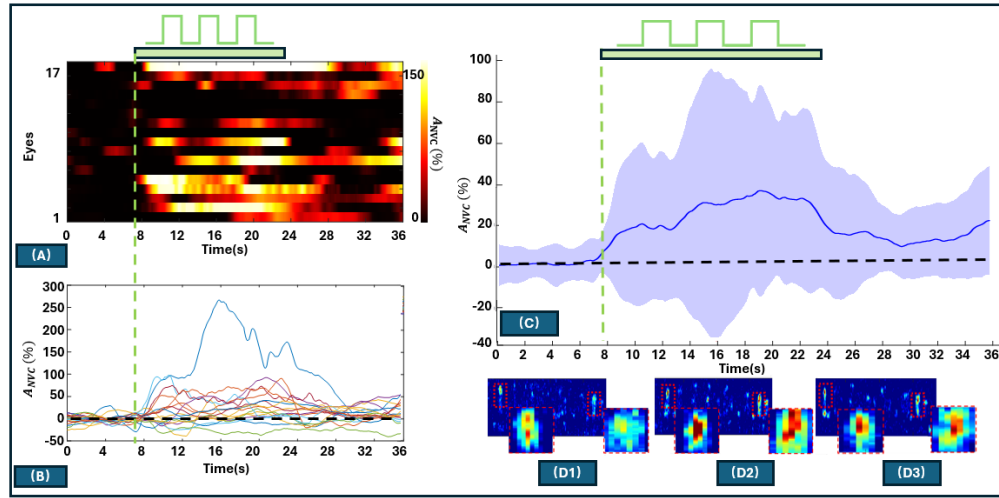


**Fig. 6. Visualization of NVC-driven hemodynamics.** (A)-(B) NVC curve visualization using a heatmap (A) and color-coded plots (B) jointly demonstrating individual inner retina's NVC amplitude ( $A_{NVC}(t)$ ) in response to stimulation (green pulse bar with the dashed line marked start). (C) Averaged curves depicting the NVC pattern of the measured group with mean value (blue curve) and SD (shaded region). (D1)-(D3) Representative OCTA B-scans showing the change of flow velocity and vasodilation in baseline (D1), stimulation (D2), and post-stimulation (D3), aligning with the NVC pattern in (C).

increased during stimulation, then gradually decreased post-stimulation, remaining slightly above the baseline. Additionally, time-to-peaks of each pattern were clearly visualized, revealing similar temporal responses of NVC across vascular plexuses.

### 3.4. Statistics of NVC amplitude and time-to-peak

We obtained the mean NVC amplitude for each individual eye in each evaluation session. A total of 15 eyes were statistically analyzed with NVC amplitude and time-to-peak metrics (mean  $\pm$  SD) (Table 1, Fig. 8(A)). Overall, the NVC amplitude showed a significant increase during stimulation, post-stimulation, and both sessions combined in all plexuses. Specifically, the NVC amplitude progressively increased from the SVC to the ICP and was highest in the DCP (Fig. 8(A)). NVC amplitude changes were highly significant along sessions in all plexuses except SVC, which was not significant (Table 1; One-way ANOVA). Time-to-peak data indicated that the different plexuses responded to stimulation within a similar time course (Table 1, Fig. 8(B)).

**Table 1. Quantification of NVC response (Mean  $\pm$  SD) in the inner retina, SVC, ICP, and DCP.<sup>a</sup>**

Mean $\pm$ SD	NVC Amplitude			One-way ANOVA ( $P$ values)	Time-to-peak
	Stimulation	Post-stimulation	Both Sessions		
Inner Retina	18.53% $\pm$ 19.54%	12.80% $\pm$ 11.93%	16.29% $\pm$ 14.18%	6.12 <sup>b</sup>	9.36s $\pm$ 4.44s
SVC	9.72% $\pm$ 20.11%	9.88% $\pm$ 11.34%	9.94% $\pm$ 16.51%	1.93	9.21s $\pm$ 4.68s
ICP	18.64% $\pm$ 20.57%	15.13% $\pm$ 11.21%	17.27% $\pm$ 14.65%	6.25 <sup>b</sup>	8.97s $\pm$ 4.27s
DCP	28.73% $\pm$ 29.85%	17.41% $\pm$ 21.02%	24.12% $\pm$ 19.34%	6.10 <sup>b</sup>	8.90s $\pm$ 4.30s

<sup>a</sup>NVC: Neurovascular coupling; SD: Standard deviation; SVC: Superficial vascular complex; ICP: Intermediate capillary plexus; DCP: Deep capillary plexus.

<sup>b</sup> $P$  value  $< 0.05$ .



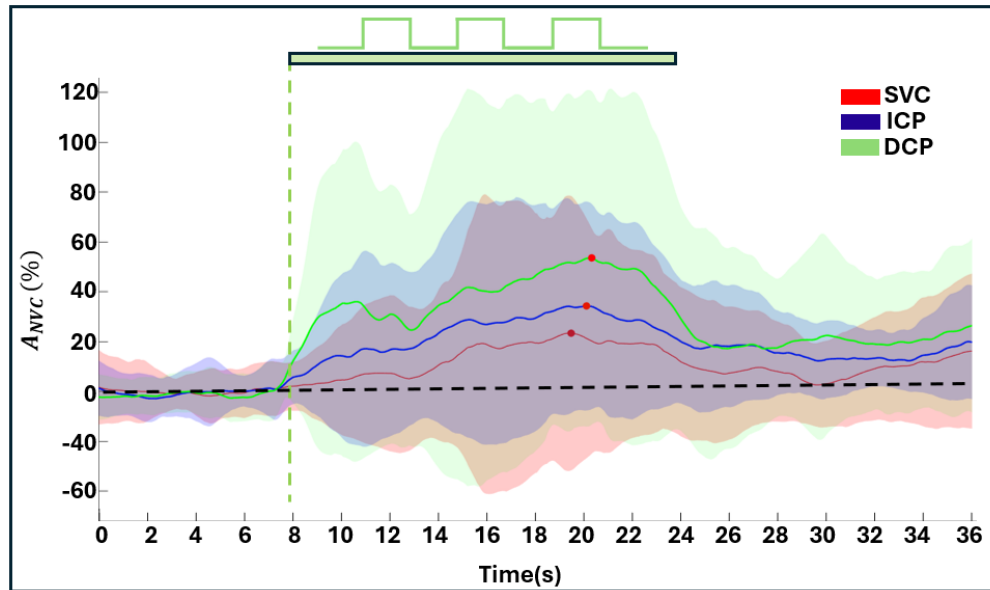


**Fig. 7. Plexus-specific NVC patterns in normal eyes.** NVC patterns illustrating differences in amplitude ( $A_{NVC}(t)$ ) and time-to-peaks (red dots on each curve) among the superficial vascular complex (red curve and shaded region, SVC), intermediate capillary plexus (blue curve and shaded region, ICP), and deep capillary plexus (green curve and shaded region, DCP) in response to green light stimulation (green pulse bar with dashed line marked start). All plexus amplitudes increase during stimulation, then gradually decrease post-stimulation, staying above the baseline (dashed black line at 0%). Time-to-peaks are highly consistent across plexuses.

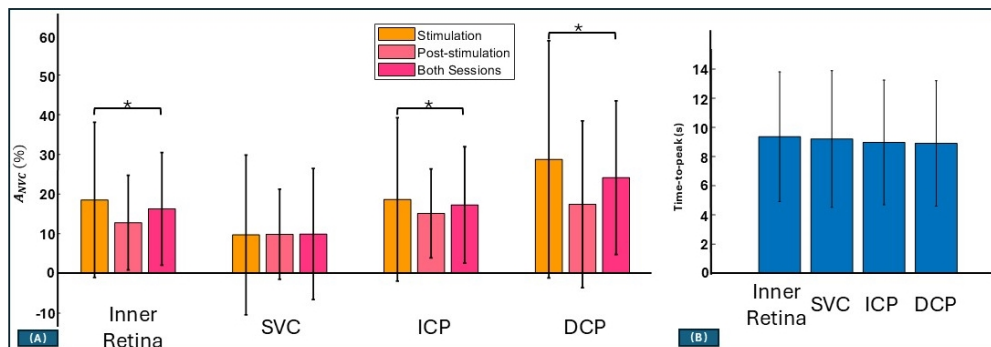


**Fig. 8. Quantification of neurovascular coupling (NVC) response.** (A) Bar plots depicting the mean NVC amplitude ( $A_{NVC}$ ) among the inner retina, superficial vascular complex (SVC), intermediate capillary plexus (ICP), and deep capillary plexus (DCP) across different sessions. Mean amplitude increased from the SVC to the ICP and further in the DCP. (B) Bar plots of time-to-peak showing the similarities in temporal response between vascular plexuses.

#### 4. Discussion

This pilot study introduces a novel hemodynamic measurement method integrating a circular-scan pattern and OCTA data post-processing to evaluate NVC at commercial OCTA speed. Our approach visualized individual NVC-driven hemodynamics and revealed plexus-specific NVC

patterns. To the best of our knowledge, this is the first study to assess parafoveal plexus-specific NVC with high temporal resolution in the human eye, laying the groundwork for future applications.

A key innovation of our approach is the implementation of a novel circular-scan pattern to generate OCTA cross-sections at a high-temporal resolution of 250-Hz. This high frame rate enables more continuous hemodynamic measurement and improves tolerance to microsaccades and blinks. First, it allows for more precise temporal characterization of the NVC response, such as accurate time-to-peak measurements, which are difficult to obtain using conventional volumetric-scan pattern [10,13]. Second, our quantitative analysis shows that the circular-scan pattern is more robust to eye movement compared to the line-scan pattern. Additionally, by encompassing all small vessels in the parafoveal region, the circular-scan enhances the sensitivity to NVC-driven hemodynamic changes. More importantly, the parafoveal region sampled by this scan is strongly associated with central vision in the human eye, making NVC assessment in this area a promising surrogate for evaluating visual function.

The advantages of our data post-processing further refine the sensitivity and accuracy of NVC evaluation. In the data post-processing, the OCT time course was used as the reference for image registration and segmentation, while the OCTA time course recording motion contrast was employed to identify and remove artifacts. Using such dual modality in post-processing significantly improves data quality. Moreover, the OCTA artifacts removal step using the histogram approach [19] improves the identification of artifacts, suppressing spike noise in the NVC response curve. Other enhancements we investigated include cross-sectional vessel masking [10] to reduce decorrelation noise, a phase-stabilized complex-based algorithm [18] for improved dynamic range, and OCTA projection artifact removal [22]. These optimizations collectively enhance the reliability of NVC evaluation.

Observed individual differences in NVC highlight the importance of high-temporal resolution, which improves accuracy in evaluating NVC amplitude and time-to-peak. Individual differences may be related to variations in photopigment profiles, and the absence of NVC amplitude increases observed in two eyes may be associated with photopigment loss. OCTA cross-sections illustrate NVC-driven hemodynamics at the single-vessel level, demonstrating that the cross-sectional method is desired for anisotropic vessel change analysis [23]. However, the role of flow velocity change in NVC requires further investigation, as the current OCTA interval is still insufficient for velocimetry [24].

Plexus-specific NVC evaluation reveals an increase in NVC amplitude with increasing depth, with the highest amplitude observed in the DCP. This may be because the eye underwent dark adaptation. After dark adaptation, the eyes can become more sensitive to the intensity of the green light stimulus than to higher-level visual information such as edges, color, and motion [25]. Bipolar cells, supplied by the DCP, respond to light intensity [26], whereas ganglion cells, supplied by the SVC, respond to processed information more than light intensity [27]. A pattern reversal where the NVC in the SVC is more affected than the DCP may be seen in diseases that primarily affect the ganglion cells, such as glaucoma or optic neuropathy [10]. The photoreceptors receive most of its blood flow from the choroidal circulation [28] and its early degeneration might be indicated by NVC evaluation of choroidal circulation, but that would not be detected by the scanning pattern of this study.

NVC evaluation might be clinically utilized to detect that dysfunction before anatomic change is observed with standard OCT. Additionally, the similarity in time-to-peak across plexuses implies NVC is triggered simultaneously in healthy eyes, analogous to normal NVC patterns in mice [29], while a delayed peak or a weak NVC amplitude increase could indicate NVC impairment in the early degeneration.

This study has several limitations. First, circular OCTA B-scanning provides limited spatial information about NVC in the capillary plexuses, where hemodynamics may be more complex

in 3D [29]. Second, our plexus-specific evaluation averages the vessel masks in each plexus slab, which helps mitigate cardiac pulsation effects and enhances NVC sensitivity but does not differentiate between arterioles and venules. Since arterioles and venules differ in their NVC [7], this can be the factor of greater NVC amplitude variation observed. In addition, our system lacks eye-tracking techniques like defocus compensation and position tracking, causing a decrease in imaging quality during prolonged imaging in NVC evaluation [30].

Future studies will integrate eye-tracking to improve focusing stability. Additionally, eye examinations, such as color vision testing, are needed to help clarify the absence of NVC increases in certain eyes. Improving the optical alignment between the stimulus and fixation target helps accommodate inter-subject variability in ocular optics. More OCTA repeats could be added to enhance the dynamic range and sensitivity to flow velocity changes. In post-processing, arteriole- and venule-specific NVC responses could be analyzed, and artifact and OCTA projection removal could be refined and quantitatively validated. Lastly, reducing NVC evaluation duration will improve clinical feasibility, and pupil dilation may enhance trial-to-trial repeatability in subjects with pronounced pupillary light reflex.

## 5. Conclusion

NVC evaluation with circular-scan OCTA enabling high-temporal resolution can characterize functional features such as amplitude and time-to-peak, which could prove useful for early detection of degenerative diseases like diabetic retinopathy and age-related macular degeneration. In this pilot study, we adapted existing OCTA techniques for human eye NVC evaluation, making it more feasible, commercially viable, and clinically translatable beyond research settings. Through hardware and software enhancements to correct artifacts, improve sensitivity, and mitigate eye movement effects, we visualized and quantified NVC-driven hemodynamics in normal eyes at a plexus-specific level for the first time. We will also realize that improving the utility of NVC evaluation requires collective efforts in scientific validation, advanced imaging techniques, and a deeper understanding of etiology and pathophysiology. Further advancements in these areas will help maximize the potential of NVC biomarkers for better clinical outcomes.

**Funding.** National Institutes of Health (R01 EY 036429, R01 EY 035410, R01 EY 024544, R01 EY 027833, R01 EY 031394, R43 EY 036781, P30 EY 010572, T32 EY023211, UL1TR002369); Jennie P. Weeks Endowed Fund; Unrestricted Departmental Funding Grant and Dr. H. James and Carole Free Catalyst Award from Research to Prevent Blindness; Malcolm M. Marquis, MD Endowed Fund for Innovation; Edward N. and Della L. Thome Memorial Foundation; Bright Focus Foundation (G2020168, M20230081).

**Disclosures.** T.T. Hormel: Ifocus Imaging (I); D. Huang: Visionix/Optvue (F, P, R), Boeringer Ingelheim (C), Roche/Genentech (P, R), Cylite (F), Intalight (F), Kugler (R), Elsevier (R), GoCheck Kids (I, P), Stroma (I), Unfold Therapeutics (I, P); S.T. Bailey: Visionix/Optovue (F); Y. Jia: Optovue/Visionix (P, R), Genentech/Roche (P, R, F), Ifocus Imaging (I, P), Optos (P), Boeringer Ingelheim (C), Kugler (R). These potential conflicts of interest have been reviewed and managed by OHSU. Other authors declare no conflicts of interest related to this article.

**Data availability.** Data underlying the results presented in this paper are not publicly available at this time but may be obtained from the authors upon reasonable request.

## References

1. J. Kur, E. A. Newman, and T. Chan-Ling, "Cellular and physiological mechanisms underlying blood flow regulation in the retina and choroid in health and disease," *Prog. Retinal Eye Res.* **31**(5), 377–406 (2012).
2. C. Iadecola, "The neurovascular unit coming of age: a journey through neurovascular coupling in health and disease," *Neuron* **96**(1), 17–42 (2017).
3. Q. S. You, J. Wang, Y. Guo, *et al.*, "Detection of reduced retinal vessel density in eyes with geographic atrophy secondary to age-related macular degeneration using projection-resolved optical coherence tomography angiography," *Am. J. Ophthalmol.* **209**, 206–212 (2020).
4. G. Garhöfer, J. Chua, B. Tan, *et al.*, "Retinal neurovascular coupling in diabetes," *J. Clin. Med.* **9**(9), 2829 (2020).
5. K. Polak, L. Schmetterer, and C. E. Riva, "Influence of flicker frequency on flicker-induced changes of retinal vessel diameter," *Investigative Ophthalmology & Visual Science* **43**, 2721–2726 (2002).
6. A. I. Srienc, Z. L. Kurth-Nelson, and E. A. Newman, "Imaging retinal blood flow with laser speckle flowmetry," *Front. Neuroenerg.* **2**, 128 (2010).

7. R. L. Warner, A. De Castro, L. Sawides, *et al.*, “Full-field flicker evoked changes in parafoveal retinal blood flow,” *Sci. Rep.* **10**(1), 16051 (2020).
8. S. Fragiotta, M. D. Pinazo-Durán, and G. Scuderi, “Understanding neurodegeneration from a clinical and therapeutic perspective in early diabetic retinopathy,” *Nutrients* **14**(4), 792 (2022).
9. R. F. Spaide, J. G. Fujimoto, N. K. Waheed, *et al.*, “Optical coherence tomography angiography,” *Prog. Retinal Eye Res.* **64**, 1–55 (2018).
10. E. Wei, Y. Jia, O. Tan, *et al.*, “Parafoveal retinal vascular response to pattern visual stimulation assessed with OCT angiography,” *PLoS One* **8**(12), e81343 (2013).
11. P. Zang, G. Liu, M. Zhang, *et al.*, “Automated motion correction using parallel-strip registration for wide-field en face OCT angiogram,” *Biomed. Opt. Express* **7**(7), 2823–2836 (2016).
12. S. Chen, S. Ni, A. Jiménez-Villar, *et al.*, “Optical coherence tomography split-spectrum amplitude-decorrelation optoretinography,” *Opt. Lett.* **48**(15), 3921–3924 (2023).
13. M. Kallab, N. Hommer, B. Tan, *et al.*, “Plexus-specific effect of flicker-light stimulation on the retinal microvasculature assessed with optical coherence tomography angiography,” *Am. J. Physiol. Heart Circ. Physiol.* **320**(1), H23–H28 (2021).
14. J. M. Provis, A. M. Dubis, T. Maddess, *et al.*, “Adaptation of the central retina for high acuity vision: cones, the fovea and the avascular zone,” *Prog. Retinal Eye Res.* **35**, 63–81 (2013).
15. X. Wei, T. T. Hormel, Y. Guo, *et al.*, “75-degree non-mydratic single-volume optical coherence tomographic angiography,” *Biomed. Opt. Express* **10**(12), 6286–6295 (2019).
16. N. Huang, T. T. Hormel, G. B. Liang, *et al.*, “Optimizing numerical k-sampling for swept-source optical coherence tomography angiography,” *Opt. Lett.* **49**(5), 1201–1204 (2024).
17. X. Wei, A. Camino, S. Pi, *et al.*, “Fast and robust standard-deviation-based method for bulk motion compensation in phase-based functional OCT,” *Opt. Lett.* **43**(9), 2204–2207 (2018).
18. X. Wei, T. T. Hormel, and Y. Jia, “Phase-stabilized complex-decorrelation angiography,” *Biomed. Opt. Express* **12**(4), 2419–2431 (2021).
19. A. Camino, Y. Jia, G. Liu, *et al.*, “Regression-based algorithm for bulk motion subtraction in optical coherence tomography angiography,” *Biomed. Opt. Express* **8**(6), 3053–3066 (2017).
20. C. Ellis, “The pupillary light reflex in normal subjects,” *Br. J. Ophthalmol.* **65**(11), 754–759 (1981).
21. T. T. Hormel, Y. Jia, Y. Jian, *et al.*, “Plexus-specific retinal vascular anatomy and pathologies as seen by projection-resolved optical coherence tomographic angiography,” *Prog. Retinal Eye Res.* **80**, 100878 (2021).
22. T. T. Hormel, D. Huang, and Y. Jia, “Artifacts and artifact removal in optical coherence tomographic angiography,” *Quant. Imaging Med. Surg.* **11**(3), 1120–1133 (2020).
23. X. Yao, T. Adejumo, T. Son, *et al.*, “Doppler OCT verifies pulsation-induced anisotropic vessel lumen dynamics in the human retina,” (2025).
24. J. Tokayer, Y. Jia, A.-H. Dhalla, *et al.*, “Blood flow velocity quantification using split-spectrum amplitude-decorrelation angiography with optical coherence tomography,” *Biomed. Opt. Express* **4**(10), 1909–1924 (2013).
25. K.-W. Yau, “Phototransduction mechanism in retinal rods and cones. The Friedenwald Lecture,” *Investigative Ophthalmology & Visual Science* **35**, 9–32 (1994).
26. E. D. Eggers, R. E. Mazade, and J. S. Klein, “Inhibition to retinal rod bipolar cells is regulated by light levels,” *J Neurophysiol.* **110**(1), 153–161 (2013).
27. U. S. Kim, O. A. Mahroo, J. D. Mollon, *et al.*, “Retinal ganglion cells—diversity of cell types and clinical relevance,” *Front. Neurol.* **12**, 661938 (2021).
28. A. Camino, Y. Guo, Q. You, *et al.*, “Detecting and measuring areas of choriocapillaris low perfusion in intermediate, non-neovascular age-related macular degeneration,” *Neurophotonics* **6**(4), 1 (2019).
29. K. Liu, T. Zhu, M. Gao, *et al.*, “Functional OCT angiography reveals early retinal neurovascular dysfunction in diabetes with capillary resolution,” *Biomed. Opt. Express* **14**(4), 1670–1684 (2023).
30. S. S. Gao, Y. Jia, L. Liu, *et al.*, “Compensation for reflectance variation in vessel density quantification by optical coherence tomography angiography,” *Invest. Ophthalmol. Vis. Sci.* **57**(10), 4485–4492 (2016).